ARTICLE

Atom Transfer between Precision Nanoclusters and Polydispersed Nanoparticles: A Facile Route for Monodispersed Alloy Nanoparticles and their Superstructures

Received 00th January 20xx,
Accepted 00th January 20xx

DOI: 10.1039/x0xx00000x

Paulami Bose,[a] Papri Chakraborty,‡[a] Jyoti Sarita Mohanty,‡ [a] Nonappa,[b] Angshuman Ray Chowdhuri,[a] Esma Khatun,[a] Tripti Ahuja,[a] Ananthu Mahendranath,[a,c] and Thalappil Pradeep*[a]

Reactions between atomically precise noble metal nanoclusters (NCs) have been studied widely in the recent past, but such processes between NCs and plasmonic nanoparticles (NPs) have not been explored earlier. For the first time, we demonstrate spontaneous reactions between an atomically precise NC, $Au_{25}(PET)_{18}$ (PET = 2-phenylethanethiol), and polydispersed silver NPs with an average diameter of 4 nm and protected with PET resulting in alloy NPs under ambient conditions. These reactions were specific to the nature of the protecting ligands as no reaction was observed between $Au_{25}(SBB)_{18}$ NC (SBB = 4-(*tert*-butyl)benzyl mercaptan) and the very same silver NPs. The mechanism involves an interparticle exchange of the metal and ligand species where the metal-ligand interface plays a vital role in controlling the reaction. The reaction proceeds through transient $Au_{25-x}Ag_x(PET)_n$ alloy cluster intermediates as observed in time-dependent electrospray ionization mass spectrometry (ESI MS). High-resolution transmission electron microscopic (HRTEM) analysis of the resulting dispersion showed the transformation of polydispersed silver NPs into highly monodispersed gold-silver alloy NPs which assembled to form 2-dimensional superlattices. Using NPs of other average sizes (3 and 8 nm), we demonstrated that size plays an important role in the reactivity as observed in ESI MS and HRTEM.

Introduction

Well-defined plasmonic metal nanoparticles (NPs) are crucial in nanotechnology for their unique roles as catalysts in fuel cells,[1–3] electrochemical reduction of CO_2,[4,5] green chemistry,[6,7] *etc*. and as probes in biomedical diagnosis[8,9] and therapy.[10,11] These and related applications bring in challenges for synthetic methods that can offer fine control over NP size dispersity. Substantial progress has been made in developing recipes to synthesize metal NPs that could address the issue of polydispersity as well as shape selectivity at the same time.[12–17] Efforts have been made to optimize synthetic methodologies for size and shape-selective preparation of monodispersed spherical metal NPs, nanorods,[18–21] nanowires,[22] nanotriangles,[23,24] nanocubes[25] and other polygonal structures. Most of the available literature is limited to the synthesis of monodispersed particles of either gold (Au) or silver (Ag). It is well established that bimetallic Au-Ag alloys have enhanced catalytic and plasmonic performance.[26,27] Ultrafine bimetallic alloy NPs often suffer inhomogeneous alloying and aggregation due to their high surface energy and phase separation at the atomic level.[27] There are still challenges to develop strategies to synthesize ultrafine well-alloyed NPs that can offer concurrent control over size homogeneity and crystallinity. Size dispersity of NPs can significantly alter their self-assembling behavior,[28–30] material properties,[31] and device performance.[32,33] Therefore, methods have been developed to enhance their monodispersity; including solvent-selective precipitation,[34,35] centrifugation,[36] size-exclusion chromatography,[37,38] and electrophoresis.[39,40] Anti-galvanic reactions (AGR) are recently gaining popularity particularly in the preparation of atomically monodisperse bimetallic NPs where NP size is less than 3 nm. AGR studies are mostly limited to atomically precise ultrasmall NPs of less than 3 nm in size, referred to as nanoclusters (NCs).[41] To best of our knowledge, extensive studies of AGR involving larger NPs are rare. Available techniques[27,42] for ultrafine bimetallic alloy NPs are co-reduction,[43] seed-mediated growth,[44] laser ablation,[45] and galvanic replacement.[46]

In recent years, atomically precise noble metal nanoclusters (NCs) have emerged as a new family of nanomaterials with precise composition and structure, which exhibit well-defined physical, chemical and electronic properties.[47–50] Over a hundred well-defined NCs have been characterized in the recent past, and many of their properties have been examined in detail.[51–53] Of these, 2-phenylethanethiol (PET) protected gold NC, $Au_{25}(PET)_{18}$, is one of the most studied NC systems, and has been used in the present investigation.[54–57]

[a] *DST Unit of Nanoscience (DST UNS) and Thematic Unit of Excellence (TUE), Department of Chemistry, Indian Institute of Technology Madras, Chennai 600 036, India.*
[b] *Faculty of Engineering and Natural Sciences, Tampere University, P.O. Box 541, FI-33101 Tampere, Finland.*
[c] *Department of Metallurgical and Materials Engineering, Indian Institute of Technology Madras, Chennai 600036, India.*
‡ Authors contributed equally.

Electronic Supplementary Information (ESI) available: Concentration calculations, ESI MS, UV-Vis, HRTEM, MALDI MS, STEM-EDS, and Raman Spectra. See DOI: 10.1039/x0xx00000x

Extensive studies on various properties of NCs showed that they are indeed molecules.[58,59] An essential characteristic of the NC is its chemical reactivity and sensitivity towards atomic exchange. It has been demonstrated that reactions between NCs (i.e. intercluster reactions), conserving composition and structure, involving atom exchange between two different types of NCs are possible.[60] Intercluster reaction was first reported for the NC systems comprising of $Au_{25}(PET)_{18}$ and $Ag_{44}(FTP)_{30}$ where FTP refers to 4-fluorothiophenol.[61] Later on, similar reactions were observed for the $Au_{25}(PET)_{18}$ with various other NC systems, such as $Ag_{25}(DMBT)_{18}$,[60] $Ag_{51}(BDT)_{19}(TPP)_3$, and $Ag_{29}(BDT)_{12}(TPP)_4$,[62] where DMBT, BDT, and TPP refer to 2,4-dimethylbenzenethiol, 1,3-benzenedithiol, and triphenylphosphine, respectively. In a few cases, such intercluster reactions were employed to make new NC products as well.[63] For instance, $Au_{25}(PET)_{18}$ reacts with $Ir_9(PET)_6$ to give a completely new alloy NC, $Au_{22}Ir_3(PET)_{18}$ as the product, which was not synthesized earlier using the conventional synthetic protocols.[64] Metal exchanges were seen between $Au_{25}(PET)_{18}$ and $Au_{38}(PET)_{24}$ NCs with bulk metallic silver.[65]

In an effort to achieve monodispersity in NPs, a method called digestive ripening was proposed by Klabunde and Sorenson,[66] which demonstrated positive results for highly polydispersed dodecanethiol-ligated gold NPs. This method was extended to other metal systems and was explored extensively by several researchers over the years.[67–70] Digestive ripening is a post-synthetic size modification method that makes highly polydispersed particles to attain monodispersity, typically in the case of noble metal NPs, without employing any other size-separation techniques. This method is assumed to be driven by ligand mediated surface etching of larger NPs along with dissolution of smaller NPs; followed by the growth of remaining NPs as they come in contact with the etched species. Both two-dimensional (2D) and three dimensional (3D) superlattices have been prepared using this approach.[71,72] Despite its success in enhancing monodispersity, the mechanism involved has not been understood clearly. The binding strength between the NPs and the ligand, ligand-solvent compatibility and temperature were already identified as the main parameters affecting digestive ripening.[73–78]

Previously, it has been shown that tellurium nanowires decorated with Ag_{44}(*p*MBA)$_{30}$ NCs (where *p*MBA refers to *para*-mercaptobenzoic acid) form crossed bilayer assemblies driven by inter-NC hydrogen bonding.[79] Similarly, when *p*MBA coated gold nanorods were interacted with Ag_{44}(*p*MBA)$_{30}$ NCs, well-defined core-shell structures were formed.[80] It is important to note that in the above examples, the interaction between the NCs and NPs led to supramolecular assemblies directed purely *via* hydrogen bonding between the surface ligands and no metallic atom transfer reactions were involved. Therefore, the intrinsic properties of the individual components were retained in the superstructures. However, it is relevant to investigate the feasibility of chemical reactions between atomically precise NCs and plasmonic NPs. In this paper, we present the first example of a chemical reaction between Au NCs and polydispersed Ag NPs offering a unique route towards the preparation of well-defined highly monodispersed hybrid Au-Ag alloy NPs. The resulting alloy NPs further self-assemble spontaneously to a higher order superstructure. This study gives a better insight in the reaction pathways and intermediate species involved colloidal state reactions. Compared to other AGR reported till date, the merit of this method is that it allows modification in order to achieve fine control over the size and composition of bimetallic NPs and their assembly with reproducibility. The properties of resulting NPs can be altered by simply modifying the reaction with different protecting ligands. We chose PET protected polydispersed silver NPs (Ag@PET) and $Au_{25}(PET)_{18}$ NC as model systems to investigate NC-NP reactions.

We show that when gold NCs were mixed with polydispersed silver NPs, the NC-NP reactions led to highly monodispersed thermodynamically stable Ag-Au bimetallic NPs. Importantly, the newly formed monodispersed NPs underwent a higher order assembly resulting in a 2D superlattice. The transient NC species formed in the course of the reaction are alloys that have been characterized by mass spectrometry (MS). A host of microscopic and spectroscopic studies confirmed the compositional change in both the systems. We also observed that the composition of the alloy clusters formed in the process goes through time-dependent changes suggesting details of the mechanism involved. We propose that the atomic transfer between NC and NP during interparticle reactions as one of the plausible routes leading to digestive ripening. Our study also shows that such reactions are more facile with smaller NPs than with larger ones.

Experimental

Materials

Silver nitrate ($AgNO_3$, 99.9%) was purchased from Rankem Chemicals. 2-PET, 4-(*tert*-butyl)benzyl mercaptan (BBSH), sodium borohydride ($NaBH_4$, 98%), and tetraoctyl ammonium bromide (TOABr) were purchased from Sigma-Aldrich. Tetrachloroauric acid ($HAuCl_4.3H_2O$) was prepared in the laboratory starting from pure gold. All the solvents (dichloromethane, methanol, and tetrahydrofuran) used were of HPLC grade and were used without further purification. Millipore-produced deionized water (~18.2 MΩ) was used throughout the experiments.

Syntheses of Ag@PET nanoparticles

The synthesis of Ag@PET NPs was carried out by modifying the traditional preparation methods of silver NPs.[81–83] Different sizes of Ag NPs were achieved by playing with the amount of reducing agent used in the course of the reaction. In a typical synthesis, 50 mg of $AgNO_3$ was dissolved in 0.5 mL water and added to 58 µL of PET in 30 mL methanol. Subsequently, silver was reduced to the zero-valent state by slow addition of freshly prepared aqueous $NaBH_4$ solution (0.3 M, 0.2 M, and 0.1 M), made in 8 mL ice-cold water. The reaction mixture was kept under reflux at 333 K with vigorous stirring for 12 h. The resulting precipitate was collected and repeatedly washed with methanol by centrifugal precipitation. Finally, the Ag@PET NPs formed were extracted as dark brown precipitate, soluble in

DCM and DMF. High-speed centrifugation at 8000 rpm for 20 min was used to separate larger sized particles. The particles were found to be stable for weeks when stored in a refrigerator under dark but the stability decreased to 3-4 days under ambient conditions. During the optimization process, it was observed that the amount of reducing agent plays a key role in defining the size of the NPs. When the molar concentration of $NaBH_4$ was increased in the reaction mixture, smaller Ag NPs were obtained. Apart from that, temperature was found to be a crucial factor in tuning the shape of the NPs and hence, the reaction temperature was set at 333 K. Fig. S1 shows detailed characterization of the Ag NPs using HRTEM and UV-Vis spectroscopy, where characteristic plasmonic peaks were observed at 454, 442, and 453 nm for particles with mean sizes of 3.17 ± 1.5, 4.37 ± 2.3 and 8.45 ± 6.3 nm NPs, respectively, which are referred to as 3, 4 and 8 nm particles subsequently. The sizes of the particles refer to the core diameter measured by high-resolution transmission electron microscopy (HRTEM).

Synthesis of $Au_{25}(PET)_{18}$ NCs

Synthesis of the NC was performed following the reported protocol.[84,85] A solution containing 40 mg of $HAuCl_4 \cdot 3H_2O$ and 7.5 mL of THF was prepared, and to that 65 mg of TOABr was added. The mixture was stirred for 15 min until the solution turned orange red. Subsequently 68 µL of PET was added and the mixture was allowed to stir for 1 h. The as-formed Au-PET thiolate was reduced by adding a solution containing 39 mg $NaBH_4$ in ice-cold water as the color of the reaction mixture turned from yellow to orange. Now, the solution was stirred for another 5 h for complete reduction and size-focusing in order to achieve high yield of the intended NC. After 5 h, the crude NC was dried using a rotavapor and it was subjected to a methanol wash to get rid of free thiols and excess thiolates. The process was repeated multiple times to obtain a clean NC. The NC was extracted in acetone and centrifuged, the supernatant was collected, and the precipitate containing larger NCs was discarded. The supernatant, composed of the size-focused clean NC in acetone, was vacuum dried. Finally, the NC was dissolved in DCM, followed by centrifugation at 10,000 rpm, and the supernatant comprising of pure NC was collected. The purified NC was characterized using UV-Vis spectroscopy and ESI MS (Fig. S2).

Reaction of Ag@PET NPs with $Au_{25}(PET)_{18}$ NCs

For NP-NC reaction, about 7.5 mg of Ag@PET NPs were dissolved in 3 mL DCM (~9.05 µM) and about 0.9 mg of $Au_{25}(PET)_{18}$ NC was dissolved in 300 µL of DCM (~7.67 µM, concentration in the final reaction mixture), separately. Concentrations mentioned are in terms of the metal present. The two dispersions were mixed at room temperature and after 15 min, about 100 µL of the reaction mixture was taken and further diluted in 0.5 mL of DCM. The solution was characterized using HRTEM and UV-Vis spectroscopy. Allowing the reaction to continue for a longer time (of the order of hours) resulted in slow precipitation (black in color) with the supernatant turning colorless. The concentration calculations are presented in the supplementary information.

Sample preparation for ESI MS experiments

Firstly, about 75.99 µM solution of the NC was prepared by dissolving 8.1 mg of $Au_{25}(PET)_{18}$ in 3 mL of DCM. Another, Ag@PET NP dispersion of ~9.05 µM was prepared with 7.5 mg of NPs in 3 mL DCM. Then, to the NC solution, 300 µL of Ag NP (~0.82 µM, concentration in the final reaction mixture) dispersion was added. The reaction was monitored using a stopwatch which was started immediately as the NP was added. After 2 min of reaction, 0.25 mL of the reaction mixture was pipetted out and diluted with 0.25 mL of DCM, and was cooled in an ice-bath. The time interval specified is the time at which the pipetted out reaction mixture was dipped in the ice-cold condition. The cooling down of the reaction mixture slowed down the reaction rate but did not quench it completely. The reaction mixture was then centrifuged and the supernatant was studied using ESI MS. The same was repeated at 3, 4, 5, 7, and 10 min intervals. After 15 min, the left-over reaction mixture was centrifuged and the black precipitate was subjected to HRTEM imaging.

Synthesis of $Au_{25}(SBB)_{18}$ NCs

The NC was synthesized according to our already reported protocol.[86] In a round bottom flask, about 10 mL of $HAuCl_4 \cdot 3H_2O$ (14.5 mM in THF) was taken and then 15 mL 4-(*tert*-butyl)benzyl mercaptan (BBSH) (89.2 mM in THF) was added while stirring at 400 rpm at room temperature. The solution turned colorless after 15 min, indicating the formation of Au(I)SBB thiolate. This was followed by a rapid addition of 2.5 mL aqueous solution of $NaBH_4$ (0.4 M) to the reaction mixture under vigorous stirring (1100 rpm). The solution turned colorless to black, indicating the formation of NCs. The reaction mixture was allowed to stir for 3 h in ambient conditions and then for another 3 h at 318 K for complete conversion. The solution was left overnight for size focusing. The product was vacuum dried and the residue was washed repeatedly with 1:1 water: methanol mixture to remove excess BBSH and other side products. The $Au_{25}(SBB)_{18}$ NC was then precipitated, dried and used for further experiments.

RESULTS AND DISCUSSION

Characterization of the starting materials

To study the interparticle reaction between polydispersed silver NPs and atomically precise gold NCs, Ag@PET NPs and $Au_{25}(PET)_{18}$ NC were chosen as model systems initially. Stability of the mentioned systems made us select them for the study. Initially, three differently sized Ag@PET NPs were synthesized using the protocol discussed in the experimental section. The Ag@PET NPs were characterized using optical absorption spectroscopy (UV-Vis) and HRTEM (Fig. S1A, B, C). Three discrete sets of the synthesized Ag NPs of average diameters 3, 4, and 8 nm showed plasmonic features in UV-Vis at 454, 442,

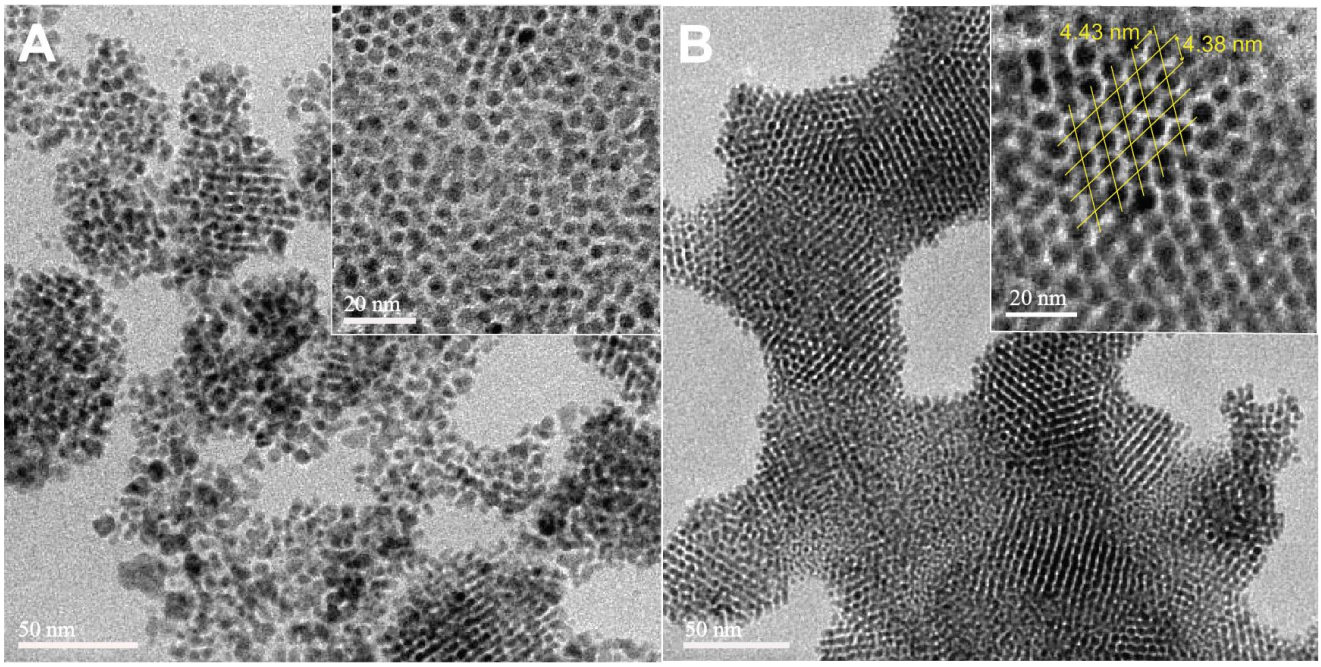

Fig. 1 HRTEM micrographs of (A) 4 nm silver NPs protected by 2-PET, and (B) spontaneously assembled NPs after the parent NPs were subjected to react with $Au_{25}(PET)_{18}$ NC.

and 453 nm, respectively (Fig. S1D), see the experimental section for more details.

The atomically precise $Au_{25}(PET)_{18}$ NC was characterized using UV-Vis which showed the characteristic peaks at 675 and 450 nm (Fig. S2A) and ESI MS measurements showed the molecular peak at m/z 7391 (Fig. S2B). The characteristic isotopic distribution further confirmed the composition of the NC.

Reaction between Ag@PET NPs with $Au_{25}(PET)_{18}$ NC

The reaction between Ag@PET NPs and $Au_{25}(PET)_{18}$ NC was achieved by mixing known volumes of the respective solutions in DCM at room temperature (see experimental section). To monitor the progress of the reaction, after 15 min, the reaction product was analyzed under HRTEM. These micrographs showed that the NP and the NC mixture resulted in highly monodispersed NPs (Fig. 1B), compared to the initial polydispersed Ag@PET NPs (Fig. 1A). More large area images from HRTEM are provided in Fig. S3 and the corresponding UV-Vis spectra in Fig. S4. The UV-Vis spectrum of the reaction product shows clearly a red-shifted surface plasmon resonance (SPR) peak at 480 nm which happens to be a characteristic feature of bimetallic Au-Ag NPs (details in later part of the manuscript).[43] The particle size distribution (Fig. S5) also underwent a transformation from 4.37 ± 2.3 nm (Fig. S5A) in the case of parent silver NPs to 3.45 ± 1.2 nm (Fig. S5B) after the reaction. This can be correlated to the changes that usually happen during high temperature annealing of particles in the process of digestive ripening.[67]

Both the parent NP and the NC were initially dispersed in DCM, and upon mixing, the assembly of NPs occurred spontaneously, and the reaction product underwent slow precipitation when left undisturbed. The product dispersed in DCM was drop-casted on a copper-grid for HRTEM studies. The reacted NPs were self-assembled into hexagonal close packed (*hcp*) 2D superlattice with an interparticle distance (denoted by "a") of 4.48 nm and a periodicity (denoted by "d") of 4.23 nm (calculated using the formula, d = $\sqrt{3}/2\ a$).[87] While the parameters, "a" and "d" include the monolayers, particle diameters determined from HRTEM refer only to the core. The parent Ag@PET NPs had a lattice fringe of 2.1 Å which corresponds to the (111) plane of silver. Upon reaction, the lattice fringe remained unaltered at 2.1 Å accompanied by the altered size of the NP. Ag@PET NPs were characterized by Raman spectroscopy before and after reaction. All the peaks of the spectra were assigned with the help of literature which confirmed the presence of PET ligand before and after reaction of Ag NPs.[88] Spectral peak assignments are presented in Fig. S6. Reduced signal intensity of the 1586 cm^{-1} peak (from 120 to 30 counts) was an indication of the reduced surface enhanced Raman activity of the reacted particles. Reduction in size led to reduced plasmonic nature of NPs which was evident from the HRTEM images. Composition has changed as well. A similar pattern of *hcp* superlattices in the case of crystalline Ag NPs were reported by Whetten *et.al*.[89] Moreover, there exists reports on gold NPs organizing to form *hcp* superlattices.[70]

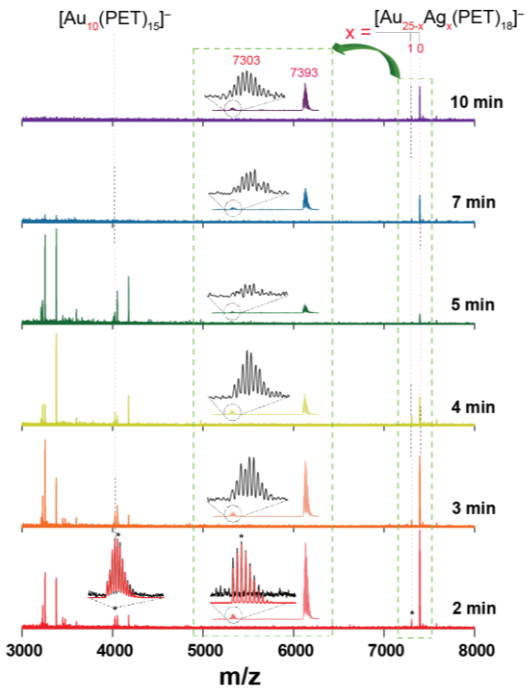

Fig. 2 Time-dependent ESI MS spectra of the reaction product identified the intermediate species, $Au_{24}Ag(PET)_{18}$ along with the evolution of the parent NC, $Au_{25}(PET)_{18}$ at m/z 7303 and 7393, respectively. Calculated (red) and experimental (black) high resolution isotopic distribution patterns (marked in *) of $Au_{24}Ag(PET)_{18}$ and $Au_{10}(PET)_{15}$ (m/z 4027) are provided for the 2 min interval spectrum. The spectral region of m/z 7280-7410 is expanded as inset.

To analyse a reaction from the perspective of the nanoparticle, there are a few *in-situ* characterization techniques, like *in-situ* scanning transmission electron microscopy (STEM)[90] and *in-situ* small-angle X-ray scattering (SAXS),[91] which can monitor the NP nucleation and growth, which can also provide mechanistic insights. The main challenges with these measurements are their limited time resolution, short observation time, damage arising from the electron beam and high experimental cost. However, in order to avoid such complications, we attempted to understand the chemical changes during the reaction using different mass spectrometric techniques. However, initial experiments with MALDI MS were not successful because there was no NC left in the reaction medium when monitored after 2 min of reaction (Fig. S7). This was attributed to the fact that the NC concentration was low and it was consumed completely during the reaction. Therefore, to monitor the changes occurring to the NC during the reaction, the initial composition (NPs:NCs = 9.05 µM:7.67 µM, in terms of the metal) was altered with a higher concentration of NCs and a lower concentration of NPs (NCs:NPs = 75.99 µM:0.82 µM, in terms of the metal). Subsequent ESI MS measurements were carried out using this composition (Fig. 2). As described above in the experimental section, after 15 min of reaction, the solution was centrifuged and the black precipitate was subjected to HRTEM studies. HRTEM micrographs suggested that upon changing the composition of the reaction (refer to the experimental section), no significant changes were seen in the product morphology (Fig. S8). The arrangement of reacted particles was slightly disturbed as a result of centrifugation in the process of separating the product from the excess NC. The reacted NPs showed an average size of 3.45 nm in precipitate which is in agreement with the initial experiments. We also conducted a concentration dependent experiment (Fig. S9) where the concentration of Ag@PET NP was kept constant while the overall concentration of $Au_{25}(PET)_{18}$ NC was varied. Firstly, stock solutions of 75.99 µM $Au_{25}(PET)_{18}$ NC and 9.05 µM Ag@PET NPs were prepared (as mentioned in the experimental section). To the Ag@PET NP dispersion, aliquots of 300 µL NC solution were added, and analyzed with HRTEM (Fig. S9A, B, C) and UV-Vis spectroscopy (Fig. S9D). Upon addition of the first aliquot of 300 µL NC, the UV-Vis spectrum (Fig. S9D, red trace) mimicked the initial observations (Fig. S4, blue trace), and the HRTEM micrographs (Fig. S9A) appeared similar to the initial particles (Fig. 1B). As the volume of the NC was increased in the reaction mixture, HRTEM micrographs (Fig. S9B, C) showed the presence of a superlattice and NC in a decreasing and increasing trend, respectively. Similarly, in the UV-Vis spectrum (Fig. S9D), the reaction mixture was similar to that of $Au_{25}(PET)_{18}$ NC (Fig. S2A). This observation led to the conclusion that the reaction was stoichiometric (all concentrations are in terms of the metal) in nature. From the above observations, it can be assumed that the reacted NP superlattices were formed when the reactants were mixed in a stoichiometric ratio (NCs:NPs = 1:1.18, in terms of the metal) and in the presence of excess $Au_{25}(PET)_{18}$, NC remained unreacted in the medium.

To understand the mechanistic details of the reaction, time dependent ESI MS was performed for the reaction of 4 nm Ag@PET NPs with $Au_{25}(PET)_{18}$ NC (refer to the experimental section). All the mass spectrometric parameters were kept

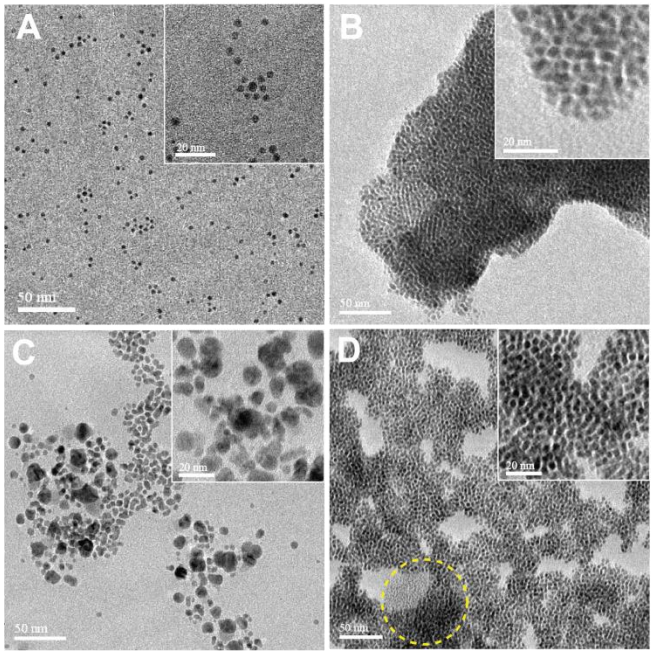

Fig. 3 Size dependence of silver NPs on the spontaneous assembly. HRTEM images (left to right) showing Ag@PET NPs before and after reaction. Silver NPs with an average size of (A) highly uniform 3 nm, and (B) assembly of post reacted particles, and (C) highly polydispersed 8 nm particles followed by (D) assembly post reaction. A second kind of assembly was observed in D (yellow circle); more images are presented in supplementary information (Fig. S12C). Higher magnification images of representative areas are in respective insets.

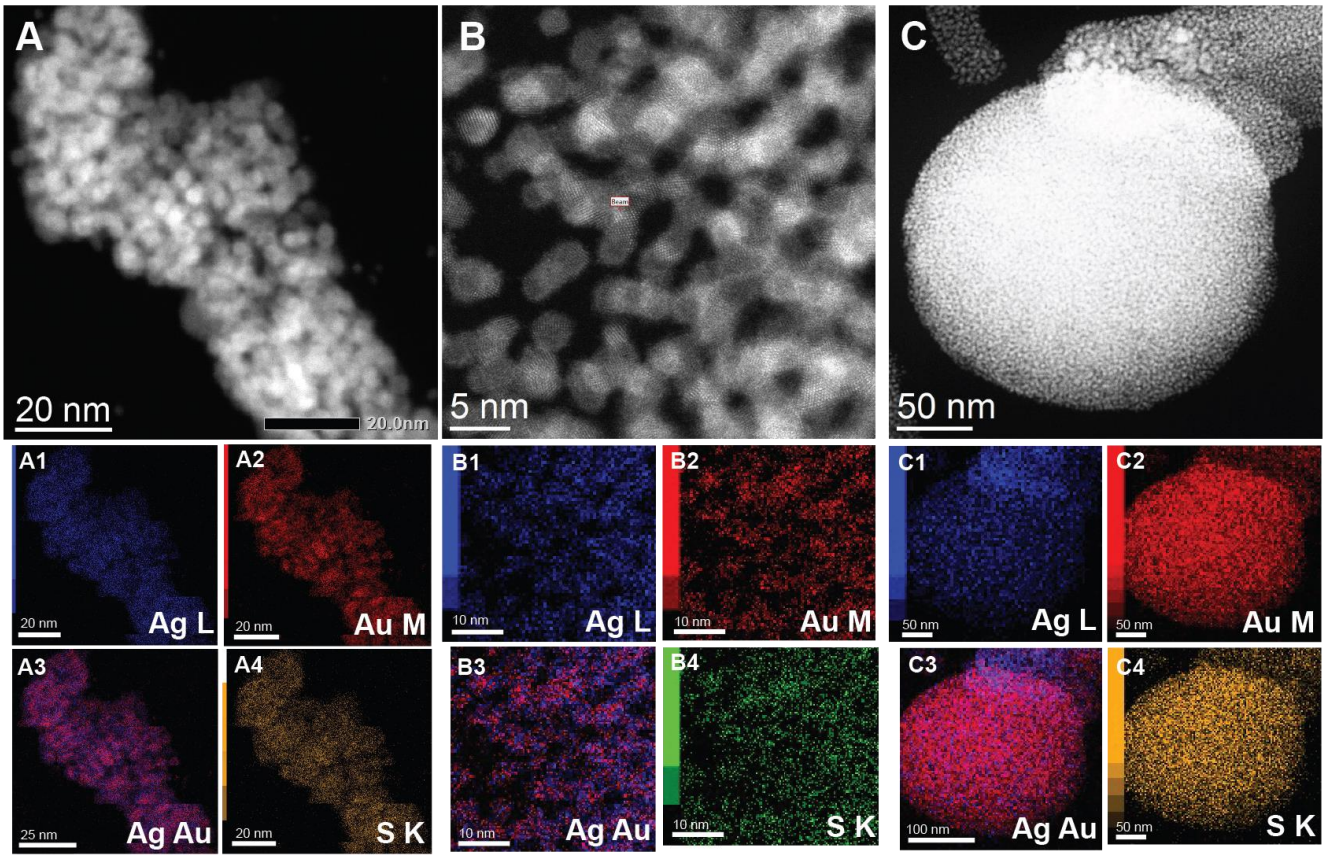

Fig. 4 Scanning transmission electron micrographs (STEM) for the (A) assembly of the reacted 4 nm Ag@PET NPs, and reacted 8 nm Ag@PET NPs arranged in (B) a planar assembly, and (C) a disc-shaped assembly. Corresponding STEM-EDS-maps of Ag, Au, Ag-Au overlay, and S are given below the STEM micrographs.

constant throughout the experiment to analyze the compositional variation of the reaction mixture with time. As shown in Fig. 2, $Au_{24}Ag(PET)_{18}$ (m/z 7303) along with a few peaks (m/z 3000-4500) corresponding to other intermediate species started to appear as early as 2 min (corresponding UV-Vis spectrum in Fig. S10). The intensity of $Au_{24}Ag(PET)_{18}$ was observed to have a fluctuating trend. $Au_{24}Ag$ was found to have a maximum lifetime in the reaction medium owing to its enhanced stability compared to other intermediate species.[92] The parent $Au_{25}(PET)_{18}$ NC (m/z 7393) showed continuous reduction in signal intensity till 5 min, followed by regeneration. Changes in the intensity of $Au_{25}(PET)_{18}$ NC can be correlated to one of the intermediates, $Au_{10}(PET)_{15}$ (m/z 4027), the generation of this species might have happened at the cost of $Au_{25}(PET)_{18}$ NC. Such short-lived species suggested that the dissociation of $Au_{25}(PET)_{18}$ NC occurred in presence of Ag@PET NPs. A time dependent plot of signal intensity (Fig. S11) of the intermediate species such as $Au_{10}(PET)_{15}$ and $Au_{24}Ag(PET)_{18}$, in comparison to that of $Au_{25}(PET)_{18}$ NC, suggested that the reaction proceeded through alloy-cluster intermediates in conjunction with NC dissociation. Occurrences of a few more thiolate-intermediates were seen in the course of the reaction. Thus, all the fragments including the alloy-NCs generated in the course of the reaction finally coalesces to form monodispersed alloy particles.

The particle size was already known as one of the primary variables of NPs, capable of modulating its chemical and physical properties.[93–96] The surface area of NPs have an inverse proportional relation with the particle size. Smaller metallic particles have a large fraction of atoms exposed, which in turn enhance their catalytic ability.[97,98] In Fig. 3, we showed that, as the size of the parent Ag NP decreases, the interparticle reaction proceeds faster. The estimated time required for the 3, 4, and 8 nm Ag NPs to react and self-assemble were around 5, 15, and 30 min, respectively. Monodispersed 3 nm sized Ag@PET NPs (Fig. 3A) underwent rapid self-assembly (Fig. 3B) upon reaction with $Au_{25}(PET)_{18}$ NC. In this case, there was a slight increase in the size (~ 3.5 nm) of the NPs post reaction (particle size distribution in Fig. S24A). To study the effect of size and polydispersity on the interparticles reactions, a batch of highly polydispersed Ag@PET NPs (Fig. 3C) with sizes ranging between 2 to 20 nm were used. When this polydispersed sample was mixed with $Au_{25}(PET)_{18}$ NC, the reaction was relatively slower compared to monodispersed NPs of other two sizes. HRTEM analysis of the reaction mixture after 30 mins revealed that NPs transformed into two different kinds of arrangements (Fig. S12), one comprised of reacted NPs of mostly 3.7 nm (Fig. 3D) and another a disc-shaped assembly extending over a diameter of about 240 nm, composed of nearly 2 nm reacted particles (Fig. S12C). The particle size distribution of post reaction samples depicted that there was a transformation of Ag NPs from high polydispersity of 8.45 ± 6.3 nm (Fig. S13A) to monodispersity of 3.73 ± 1.0 nm (Fig. S13B). This transformation of NPs from 8.45 ± 6.3 nm to 3.73 ± 1.0 nm

appears strange in terms of mass balance; however, we note that the number of particles has changed significantly in the course of the reaction. The reacted 3 and 8 nm Ag NPs were characterized using HRTEM (Fig. 3) and UV-Vis spectroscopy (Fig S25). A slightly shifted SPR peak was observed in the case of reaction of 3 nm Ag NPs (Fig. S25A); this may be attributed to the highly reactive surface Ag atoms of NP readily exchanges with Au NC, thereby attaining a rapid thermodynamic stability and the critical/equilibrium size (~ 3.5 nm) even with a lesser Au doping. On the other hand, in the case of 8 nm Ag NPs, there was a very prominent red-shifted broad SPR peak of the reaction product, centred at 556 nm (Fig. S25B). Broad SPR peaks are in agreement with the formation of higher order assembly of reacted NPs. It is widely accepted that the SPR wavelength increases with the NP size for a fixed chemical composition. However, it has been shown that the SPR is related to second-order and third order polynomial expression with the composition and size dependent coefficients, respectively. Therefore, the small shift observed for Alloy NPs obtained upon reacting 3 nm AgNPs with AuNCs is presumably due to low Au content, unlike alloys from 4 and 8 nmAgNPs. Elemental compositions of the self-assembled superstructures were analyzed using energy-dispersive X-ray spectroscopy (EDS) in a scanning transmission microscope (STEM) (Fig. 4). Elemental mapping confirmed the presence of gold, silver, sulphur and carbon in the superstructure. More importantly, the uniform distribution of gold, silver and sulphur throughout superstructures suggested that the structures that resulted on reaction were complex gold-silver hybrids. Therefore, spot EDS analysis was performed for the reacted particles, shown in Fig. 4A, obtained from parent 4 nm Ag@PET NPs, which confirmed the presence of gold (~29%) and silver (~71%) (refer to spot EDS spectrum in Fig. S14). The difference in ratios of Au and Ag between the initial mixing (Au NC: Ag NP = 1:1.18) and final resulting NPs (Au:Ag = 1:2.45) may be due to the experimental limitation where EDS mapping was attempted on a few particles in a select area against the entire range particles including byproducts, and therefore it is only a semi-qualitative method in the present case.[99–101] Then, a similar compositional analysis was performed on the self-assembled reacted particles obtained from polydispersed 8 nm Ag@PET NPs. The planar assembly showed alloy particles (Fig. 4B) with the presence of gold (~30%) and silver (~70%) (refer to spot EDS spectrum in Fig. S15). The disc-shaped assembly also confirmed to be a hybrid assembly of gold (~42%) and silver (~58%) (Fig. 4C) alloy-NPs (refer to spot EDS spectrum in Fig. S16).

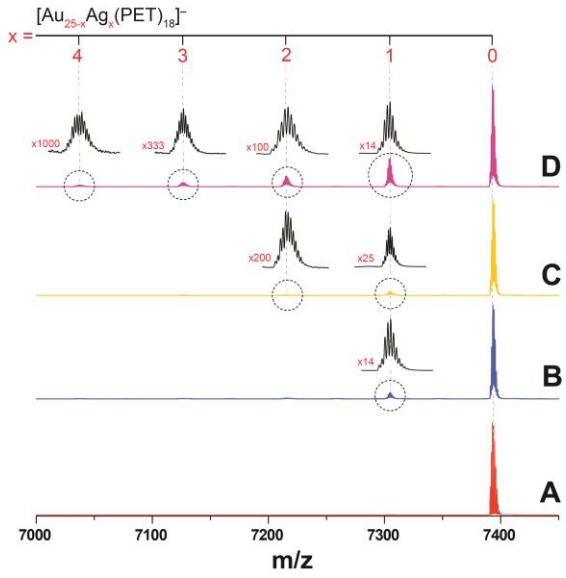

Fig. 5 Size dependent reactivity monitored using ESI MS, keeping the reaction and mass spectrometric conditions constant. The reaction was allowed for 2 min and quenched in ice-cold conditions. The rate of reaction was found to vary with the size of silver NPs. Spectra monitored after 2 min of reaction with (B) 8 nm, (C) 4 nm, and (D) 3 nm particles, and the extent of exchange was compared with the spectrum of parent (A) $Au_{25}(PET)_{18}$ NC. Spectra were normalized with the corresponding $Au_{25}(PET)_{15}$ peak intensity for visual comparison.

Fig. 5 discusses the reactivity of three differently sized NPs as the progress of the reaction was monitored with ESI MS and UV-Vis spectroscopy (Fig. S17) for the same period of time; in this case, at 2 min interval, while all experimental conditions and parent substrate concentrations were kept constant. Before the mass spectral investigation, the reactions were quenched by lowering the temperature to ice-cold conditions. For 3 nm Ag NPs (Fig. 5D), Ag_xAu_{25-x} particles were seen for x = 1, 2, 3, and 4, while for 8 nm Ag NPs (Fig. 5B) it was limited to x = 1. This reduced reactivity was reflected in all samples with larger size and greater polydispersity, consequently such samples required comparatively more time to get monodispersed. Comparative HRTEM images of the progress of the reaction for 8 nm Ag@PET NPs with time are presented in Fig. S23.

The reactions discussed above were extremely rapid and spontaneous in nature. Reactivity of the system was enhanced with the decreasing size of parent Ag NPs. Since the intermediates were short-lived, ESI MS peak intensities varied depending on the time at which reaction was quenched. In an attempt to capture the intermediates, we performed the same time-dependent reaction of 4 nm Ag@PET NPs with $Au_{25}(PET)_{18}$ NC under ice-cold conditions (Fig. S18A). The reaction was found to proceed even at a lower temperature of 273 K but at a much slower rate. The reaction mixture was subjected to ESI MS measurements from 3 min till 6 h. The intermediates continued to exist till 6 h in the ice-cold condition (Fig. S18A), which was usually 5 min for the same reaction at room temperature (Fig. S18B). In view of such reactivity, the reported intermediate signal intensities would vary slightly from the true values for a given time interval of the reaction (observed under ambient conditions).

Owing to the spontaneous nature of the NP-NC reaction, we are assuming that the NP-NC reaction is driven towards a thermodynamically stable state. A monodispersed Au-doped-Ag NP with an equilibrium size is thermodynamically more stable over its polydispersed pure monometallic state, in the reaction conditions. A thermodynamic equilibrium size of a metal NP depends on the specific protecting ligand and temperature of the reaction.[69,102,103] A thermodynamic equilibrium size is a critical size that possesses an optimum surface energy allowing a ligand-coverage in order to protect the core of metal NP from further reaction. We observed that upon interparticle reaction, when 3 nm Ag NPs were used, the

resulting alloy NPs showed an increase in their size to 3.5 nm. However, when the reaction was carried out using 5 and 8 nm Ag NPs, a decrease in the size of the alloy NPs to 3.45 and 3.7 nm, respectively were seen. Hence, we can say that, at room temperature, For PET-protected-Au-Ag bimetallic NPs, the equilibrium sizes of the NPs range between 2-5 nm and with an average of ~3.5 nm (Fig. S24). The effects of polydispersity in the shapes of Ag NPs (as evident from Fig. S1C) were reflected in the nature of the intermediates. It may be said that greater the diversity in the shapes and sizes of parent Ag NPs, larger will be the number of intermediates, as observed in ESI MS (Fig. S19B). Now, irrespective of the sizes of the parent Ag NPs, the reacted NPs get spontaneously resized to ~3.5 nm due to the reaction pathway which involves complete fragmentation and exchange of metal atoms between the particles. The process continues until a thermodynamically stable state is achieved. Digestive ripening implies the modification of both smaller and larger NPs until a preferred size is achieved. On similar lines, we are suggesting that the NP-NC reaction can be considered as one of the plausible routes of digestive ripening. Similarly, here we conclude that the smaller particles, i.e. NCs can drive particle fragmentation leading to monodispersity. This can be supported from the ESI MS experiment where a number of low mass fragments were seen in addition to alloy-NCs in the initial stages of the reaction. From all these, we propose a reaction scheme as below.

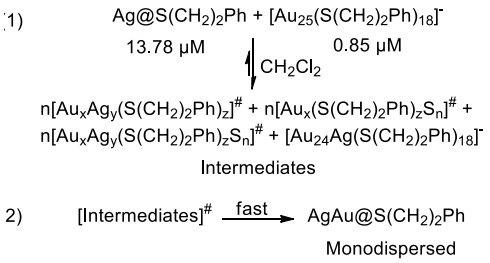

Scheme 1. Proposed chemical pathway for the reaction between Ag@PET NPs with $Au_{25}(PET)_{18}$ NC. Steps (1) Ag@PET NPs initiating alloying and fragmentation of $Au_{25}(PET)_{18}$ NC giving rise to intermediates, where x = 25, 24, 23,….., and y = 0, 1, 2, 3,….., and (2) finally the intermediates undergo mutual coalescence as well as with unreacted NPs, the reaction continues until complete consumption of $Au_{25}(PET)_{18}$ NC, and resulting in monodispersed gold-silver alloy NPs.

Monolayers on the surface of NPs have a contribution towards its chemical reactivity. We examined its influence with ESI MS (Fig. S20) as we replaced the original NC with $Au_{25}(SBB)_{18}$ NC. Here also, keeping all the experimental conditions similar, we allowed the NC to react for a span of 2 min and collected the mass spectra, where no new peaks were seen (Fig. S20A, C). Again, HRTEM (Fig. S20B, D) showed no change even after 30 min of reaction (experimental conditions as mentioned in the previous case). We failed to find any notable changes in the reaction medium unlike the one observed in the case of $Au_{25}(PET)_{18}$ NC. The results therefore suggested that the ligand also played a crucial role in such interparticle reactions. For a facile and effective reaction between a NC and NP, the metal-ligand interface played an important role as the reaction was expected to occur through the exchange of surface atoms or metal-ligand fragments.[104–106]The failure of the reaction can be attributed to a possible steric hindrance between the bulky terminal *tert*-butly group of SBB and benzene ring of PET ligands restricting the closer approach of NC to the NP surface required to initiate the reaction.

From the previous discussion, it was evident that reacted particles were arranging themselves in a specific pattern depending on the size of reacting NPs. To gain further insights on packing of the resulting NP assemblies, inverse fast Fourier transforms (IFFT) of selected images of assembles corresponding to 4 and 8 nm Ag@PET NPs were performed. 3D structural reconstructions of assemblies were carried out using electron tomography. Accordingly, a series of 2D projections were collected by tilting the sample from +69° to -69° with an increment angle of 2-3°. The tilt series was then subjected to image processing to obtain the final 3D reconstruction. As shown in Fig. 6A, superlattice assembly of the reacted 4 nm Ag@PET NPs showed an *hcp* array of particles, with an interparticle distance of ~4.5 nm (refer to square lattice in Fig. S21A). On the other hand, for the first kind of assembly derived from 8 nm Ag@PET NPs, the planar assembly (Fig. 6B) displayed a square lattice with an interparticle distance of ~4.0 nm (refer to square lattice in Fig. S21B). However, due to complex 3D multilayered assemblies (Fig. 6B), unambiguous interpretation of the assemblies based on 2D projections remained inconclusive. The second kind of assembly (Fig. S22) resulting from the same NPs turned out to be a circular disc, densely filled with reacted particles. The tilt series and 3D reconstructions for the assemblies corresponding to reacted 4 nm Ag NPs (Fig. 6A) are provided in the supplementary information as Videos V1 and V2, respectively. Also, tilt series and 3D reconstructions for the planar assembly of reacted 8 nm (Fig. 6B) are provided in the supplementary information as Videos V3 and V4, respectively.

We propose a mechanism for the reaction between Ag@PET NP and $Au_{25}(PET)_{18}$ NC. The reaction can be hypothesized to proceed through a series of events like, (i) interparticle approach, (ii) adduct formation, (iii) atomic exchange, and (iv) attaining monodispersity and consequent equilibrium. The metallophilic interaction of the Ag NP and Au NC might initiate their approach toward each other. The NC-NP reaction can be presumed to follow a host-guest reaction model similar to the enzyme-substrate model, where the NP host forms adducts with the NC guest. The flexibility of the protecting ligands on both the substrates play a major role in allowing the adduct formation. Adduct formation apparently facilitates Au-Ag atomic exchange between the two species. It was already reported that the exchange of Au-PET and Ag-PET units are facile in the case of isolobal fragments.[61] Unlike dithiols, where only metal exchange is reported, for monothiols, the metal-ligand transfer is feasible.[62] $Au_{25}(PET)_{18}$ NC undergoes atomic exchange with Ag@PET NPs to form $Au_{24}Ag(PET)_{18}$ with Ag at the center of the M_{13} core (M= metal, in this case Au) which happens to be an exceptionally stable structure.[107,108] ESI MS measurements of the ongoing reaction suggested the presence

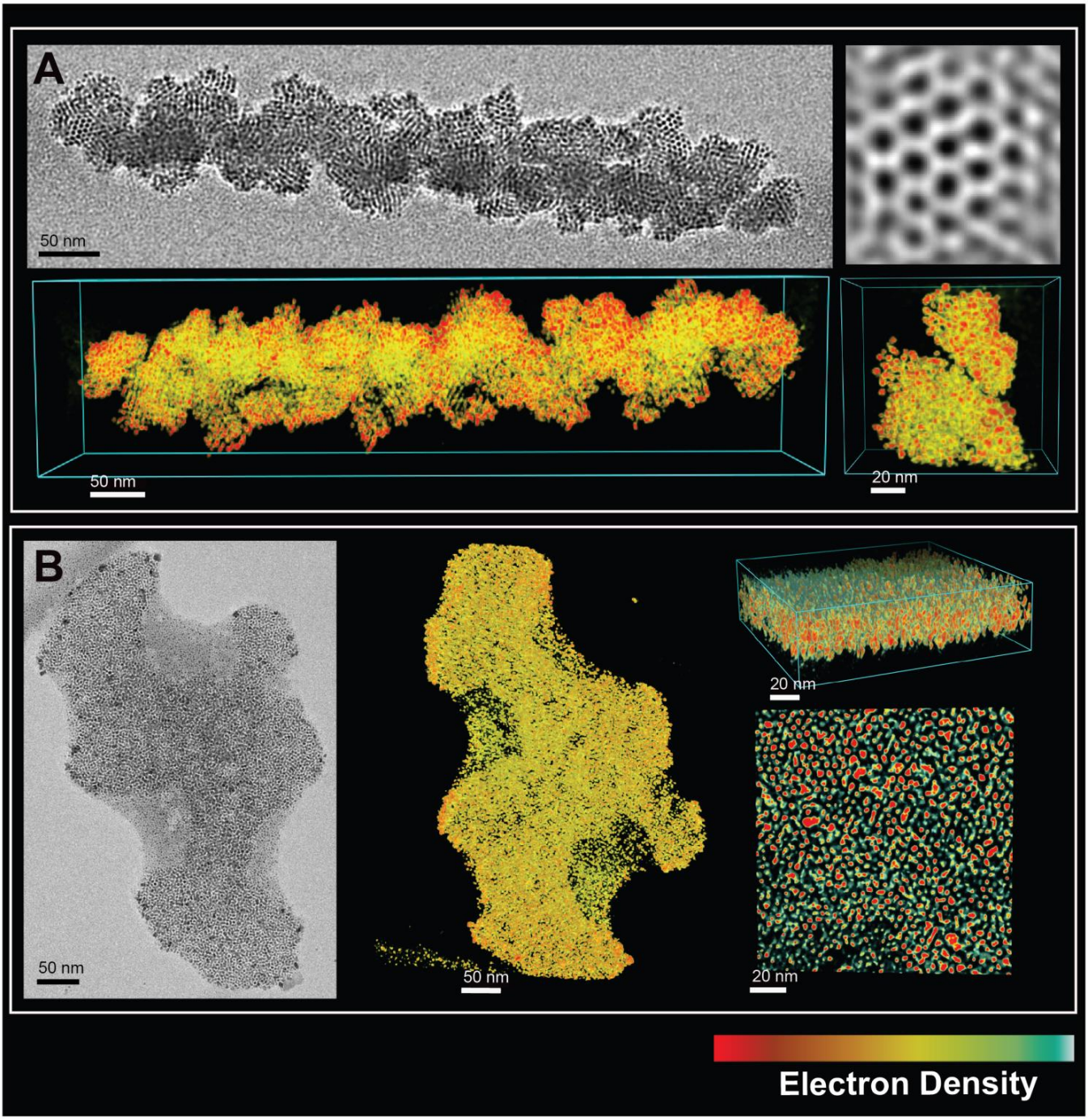

Fig. 6 Electron Tomography and 3D reconstruction: 2D projection followed by its corresponding 3D reconstruction for (A) the superlattice assembly of reacted 4 nm Ag@PET NPs and IFFT image of the *hcp* assembly, and (B) planar assembly of reacted 8 nm Ag@PET NPs.

of both multiply doped NCs as well as dissociated NC species. It can be assumed that extensive interparticle atomic exchange leads to multiple doping of the NCs, which eventually destabilized the system. In order to release this geometric strain, the NC system may undergo dissociation. The newly formed species (alloy-NC intermediates, dissociated NCs, and other low-mass fragments) in the reaction medium can now undergo coalescence mutually as well as with unreacted NPs till the system attains a stable equilibrium size. As the reactants were mixed in a ratio of NCs:NPs = 1:1.18 (in terms of the metal), the above process continues till complete consumption of $Au_{25}(PET)_{18}$ occurs.

Apart from this, the phenomenon of digestive ripening can also occur. The driving force for digestive ripening is the decrease of interfacial free energy. In a study by Hwang *et. al.*[109] on digestive ripening, the phenomenon was explained by using a modified Gibbs-Thomson equation by the introduction of an electrostatic energy factor. The equation mainly relates interfacial free energy as one of the most important factors to other physical properties, like chemical potential, particle size, and curvature factor.[110] In the case of binary systems, the

chemical potentials of both Au and Ag are important in resulting monodispersity. According to the phase diagram of an Au/Ag binary system,[111,112] Au and Ag are isomorphous with face-centered cubic (FCC) structure and therefore, it is assumed that Au and Ag NPs behave like an ideal binary solid solution. At equilibrium, the Gibbs free energy is the minimum for spherical Au-Ag binary particle compared to its pure states. The Au-Ag atomic exchange between the NPs contributes to the decrease in total Gibbs free energy. The size and compositional change due to atomic exchange between the NPs is governed by the chemical potential, which finally contributes to the minimization of the total Gibbs free energy. According to reports, solid-gas interface free energies of Ag[113] and Au[114] are 1.25 Jm^{-2} and 1.2 Jm^{-2}, respectively at their melting point. Interface free energies of Au, Ag, and Au/Ag solid-solution in the colloidal form are assumed to have a value of 0.3 Jm^{-2}. The chemical potential of Au is always higher in Au NPs than in Ag NPs. Similarly, the chemical potential of Ag is higher in Ag NPs than in Au NPs. Therefore, simultaneous diffusion of Ag from Ag NP to Au NP and Au from Au NP to Ag NP minimizes the total free energy producing monodispersed alloy NPs. We can say that doped Au or Ag NPs are thermodynamically more stable compared to its monometallic state. Inter-ligand interaction plays an important role in the formation of superlattices.[115–117] During the self-assembly of metallic NPs, the presence of strong van der Waals forces between the metallic cores brings the particles closer and at the same time the ligands (dominantly the alkyl groups) introduce an opposing interparticle steric repulsion.[118] The inter-ligand steric repulsion balanced by strong interparticle van der Waals attraction can result in a superlattice arrangement. The strong van der Waals attraction usually contributes to the ligand interdigitation between adjacent particles.[119–121]

CONCLUSIONS

In summary, we have explored the reaction of Ag NPs with atomically precise Au NCs resulting in monodispersed Au-Ag alloy NPs. Interparticle reactions are key initiators in the formation of the resultant 2D superlattice assemblies. Such interparticle reactions can be proposed as one of the methods contributing to digestive ripening of NPs. Reactions were studied for $Au_{25}(PET)_{18}$ NCs with differently sized Ag@PET NPs where we observed that the reactivity of the system was enhanced upon decreasing the size of the NPs. From our ESI MS measurements it was evident that gold-silver alloying in the case of interparticle reactions proceeded through an alloy-nanocluster intermediate followed by atomic exchange between them and subsequent NC detachment. The proposed methodology was found to contribute to achieving the highest control over NP size distribution in solutions at room temperature. The nanocluster-nanoparticle reactions can open up an entirely new method of generating uniform alloy NPs with tunable optoelectronic properties. The method may be extended to other transition metals like Ni and Fe in order to introduce properties like magnetism. Similar studies could be conducted between NPs and NCs of the same metal, resulting in monodisperse NPs without change in composition, although the present investigation were conducted with Ag NPs and Au NCs in view of the feasibility in exploring the reaction by mass spectrometry, observing the changes by EDS and STEM. In the absence of stable PET-protected Ag NC, it was not possible to extend this study presently to reaction between Au@PET and Ag NC. Further studies are progressing to understand corresponding processes with other transition metal NPs, which will be reported in due course.

Conflicts of interest

There are no conflicts to declare.

Acknowledgements

P.B., E.K., A.M., and T.A. thank IIT Madras for their research fellowships. P.C., and A.R.C. thank Department of Science and Technology (DST) for providing a postdoctoral fellowship. J.S.M. thanks the Council of Scientific and Industrial Research (CSIR) for her fellowships. We thank Manju C.K. for her help in the MALDI MS measurements, Ganesan Paramasivam for contributing with the NP and NC structures, Amrita Chakraborty, Amoghavarsha Kini, Srikrishnarka Pillalamarri and Vishal Kumar for valuable inputs in relation to this work. Academy of Finland´s Centre of Excellence in Molecular Engineering of Biosynthetic Hybrid Materials (HYBER, 2014-2019), Photonics Research and Innovation (PREIN) Flagship and Aalto University Nanomicroscopy Centre (Aalto-NMC) are acknowledged for access to their the microscopy facilities.

Notes and references

1 M. Muzzio, J. Li, Z. Yin, I. M. Delahunty, J. Xie and S. Sun, *Nanoscale*, 2019, **11**, 18946–18967.

2 F. J. Perez-Alonso, D. N. McCarthy, A. Nierhoff, P. Hernandez-Fernandez, C. Strebel, I. E. L. Stephens, J. H. Nielsen and I. Chorkendorff, *Angew. Chemie - Int. Ed.*, 2012, **51**, 4641–4643.

3 H. J. Yin, J. H. Zhou and Y. W. Zhang, *Inorg. Chem. Front.*, 2019, **6**, 2582–2618.

4 P. T. Smith, E. M. Nichols, Z. Cao and C. J. Chang, *Acc. Chem. Res.*, 2020, **53**, 575–587.

5 M. G. Kim, J. Jeong, Y. Choi, J. Park, E. Park, C. H. Cheon, N. K. Kim, B. K. Min and W. Kim, *ACS Appl. Mater. Interfaces*, 2020, **12**, 11890–11897.

6 P. Sudarsanam, E. Peeters, E. V Makshina, V. I. Parvulescu and B. F. Sels, *Chem. Soc. Rev.*, 2019, **48**, 2366–2421.

7 C. Yu, X. Guo, M. Shen, B. Shen, M. Muzzio, Z. Yin, Q. Li, Z. Xi, J. Li, C. T. Seto and S. Sun, *Angew. Chemie - Int. Ed.*, 2018, **57**, 451–455.

8 D. Ni, E. B. Ehlerding and W. Cai, *Angew. Chemie - Int. Ed.*, 2019, **58**, 2570–2579.

9 Y. Ju, H. Zhang, J. Yu, S. Tong, N. Tian, Z. Wang, X. Wang, X. Su, X. Chu, J. Lin, Y. Ding, G. Li, F. Sheng and Y. Hou, *ACS Nano*, 2017, **11**, 9239–9248.

10 L. Zhang, Q. Chen, Y. Ma and J. Sun, *ACS Appl. Bio Mater.*, 2020, **3**, 107–120.

11 Z. Shen, M. P. Nieh and Y. Li, *Polymers (Basel).*, 2016, **8**, 1–18.

12 H. M. Ashberry, J. T. L. Gamler, R. R. Unocic and S. E. Skrabalak, *Nano Lett.*, 2019, **19**, 6418–6423.

13 P. Qiu, B. Ma, C. Te Hung, W. Li and D. Zhao, *Acc. Chem. Res.*, 2019, **52**, 2928–2938.

14 Y. Yan, J. S. Du, K. D. Gilroy, D. Yang, Y. Xia and H. Zhang, *Adv. Mater.*, , DOI:10.1002/adma.201605997.

15 J. Mosquera, Y. Zhao, H. J. Jang, N. Xie, C. Xu, N. A. Kotov and L. M. Liz-Marzán, *Adv. Funct. Mater.*, 2020, **30**, 1–17.

16 C. Martín-Sánchez, A. Sánchez-Iglesias, P. Mulvaney, L. M. Liz-Marzán and F. Rodríguez, *J. Phys. Chem. C*, 2020, **124**, 8978–8983.

17 A. Vivien, M. Guillaumont, L. Meziane, C. Salzemann, C. Aubert, S. Halbert, H. Gérard, M. Petit and C. Petit, *Chem. Mater.*, 2019, **31**, 960–968.

18 G. González-Rubio, P. Díaz-Núñez, A. Rivera, A. Prada, G. Tardajos, J. González-Izquierdo, L. Bañares, P. Llombart, L. G. Macdowell, M. Alcolea Palafox, L. M. Liz-Marzán, O. Peña-Rodríguez and A. Guerrero-Martínez, *Science*, 2017, **358**, 640 LP – 644.

19 C. Martín-Sánchez, G. González-Rubio, P. Mulvaney, A. Guerrero-Martínez, L. M. Liz-Marzán and F. Rodríguez, *J. Phys. Chem. Lett.*, 2019, **10**, 1587–1593.

20 W. Ye, K. Krüger, A. Sánchez-Iglesias, I. García, X. Jia, J. Sutter, S. Celiksoy, B. Foerster, L. M. Liz-Marzán, R. Ahijado-Guzmán and C. Sönnichsen, *Chem. Mater.*, 2020, **32**, 1650–1656.

21 H. H. Chang and C. J. Murphy, *Chem. Mater.*, 2018, **30**, 1427–1435.

22 C. Jia, Z. Lin, Y. Huang and X. Duan, *Chem. Rev.*, 2019, **119**, 9074–9135.

23 L. Scarabelli, M. Coronado-Puchau, J. J. Giner-Casares, J. Langer and L. M. Liz-Marzán, *ACS Nano*, 2014, **8**, 5833–5842.

24 C. Kuttner, M. Mayer, M. Dulle, A. Moscoso, J. M. López-Romero, S. Förster, A. Fery, J. Pérez-Juste and R. Contreras-Cáceres, *ACS Appl. Mater. Interfaces*, 2018, **10**, 11152–11163.

25 S. Zhou, J. Li, K. D. Gilroy, J. Tao, C. Zhu, X. Yang, X. Sun and Y. Xia, *ACS Nano*, 2016, **10**, 9861–9870.

26 M. Rebello Sousa Dias and M. S. Leite, *Acc. Chem. Res.*, 2019, **52**, 2881–2891.

27 D. Tan, S. Tu, Y. Yang, S. Patskovsky, D. Rioux and M. Meunier, *J. Phys. Chem. C*, 2016, **120**, 21790–21796.

28 D. García-Lojo, S. Núñez-Sánchez, S. Gómez-Graña, M. Grzelczak, I. Pastoriza-Santos, J. Pérez-Juste and L. M. Liz-Marzán, *Acc. Chem. Res.*, 2019, **52**, 1855–1864.

29 Nonappa and O. Ikkala, *Adv. Funct. Mater.*, 2018, **28**, 1–14.

30 T. Udayabhaskararao, T. Altantzis, L. Houben, M. Coronado-Puchau, J. Langer, R. Popovitz-Biro, L. M. Liz-Marzán, L. Vukovic, P. Král, S. Bals and R. Klajn, *Science*, 2017, **358**, 514–518.

31 M. A. Boles, M. Engel and D. V Talapin, *Chem. Rev.*, 2016, **116**, 11220–11289.

32 J. Langer, D. J. de Aberasturi, J. Aizpurua, R. A. Alvarez-Puebla, B. Auguié, J. J. Baumberg, G. C. Bazan, S. E. J. Bell, A. Boisen, A. G. Brolo, J. Choo, D. Cialla-May, V. Deckert, L. Fabris, K. Faulds, F. Javier García de Abajo, R. Goodacre, D. Graham, A. J. Haes, C. L. Haynes, C. Huck, T. Itoh, M. Käll, J. Kneipp, N. A. Kotov, H. Kuang, E. C. Le Ru, H. K. Lee, J. F. Li, X. Y. Ling, S. A. Maier, T. Mayerhöfer, M. Moskovits, K. Murakoshi, J. M. Nam, S. Nie, Y. Ozaki, I. Pastoriza-Santos, J. Perez-Juste, J. Popp, A. Pucci, S. Reich, B. Ren, G. C. Schatz, T. Shegai, S. Schlücker, L. L. Tay, K. George Thomas, Z. Q. Tian, R. P. van Duyne, T. Vo-Dinh, Y. Wang, K. A. Willets, C. Xu, H. Xu, Y. Xu, Y. S. Yamamoto, B. Zhao and L. M. Liz-Marzán, *ACS Nano*, 2020, **14**, 28–117.

33 Z. Wang, S. Zong, L. Wu, D. Zhu and Y. Cui, *Chem. Rev.*, 2017, **117**, 7910–7963.

34 B. Kowalczyk, I. Lagzi and B. A. Grzybowski, *Curr. Opin. Colloid Interface Sci.*, 2011, **16**, 135–148.

35 K. Dey, S. Kunjattu H., A. M. Chahande and R. Banerjee, *Angew. Chemie Int. Ed.*, 2020, **59**, 1161–1165.

36 P. Li, A. Kumar, J. Ma, Y. Kuang, L. Luo and X. Sun, *Sci. Bull.*, 2018, **63**, 645–662.

37 S. Süß, V. Michaud, K. Amsharov, V. Akhmetov, M. Kaspereit, C. Damm and W. Peukert, *J. Phys. Chem. C*, 2019, **123**, 16747–16756.

38 X. X. Zhou, J. F. Liu and G. Bin Jiang, *Environ. Sci. Technol.*, 2017, **51**, 3892–3901.

39 A. Hlaváček, M. J. Mickert, T. Soukka, S. Lahtinen, T. Tallgren, N. Pizúrová, A. Król and H. H. Gorris, *Anal. Chem.*, 2019, **91**, 1241–1246.

40 B. Behdani, S. Monjezi, M. J. Carey, C. G. Weldon, J. Zhang, C. Wang and J. Park, *Biomicrofluidics*, 2018, **12**, 51503.

41 Z. Gan, N. Xia and Z. Wu, *Acc. Chem. Res.*, 2018, **51**, 2774–2783.

42 K. Loza, M. Heggen and M. Epple, *Adv. Funct. Mater.*, , DOI:10.1002/adfm.201909260.

43 M. P. Mallin and C. J. Murphy, *Nano Lett.*, 2002, **2**, 1235–1237.

44 D. Rioux and M. Meunier, *J. Phys. Chem. C*, 2015, **119**, 13160–13168.

45 R. Intartaglia, G. Das, K. Bagga, A. Gopalakrishnan, A. Genovese, M. Povia, E. Di Fabrizio, R. Cingolani, A. Diaspro and F. Brandi, *Phys. Chem. Chem. Phys.*, 2013, **15**, 3075–3082.

46 X. Xia, Y. Wang, A. Ruditskiy and Y. Xia, *Adv. Mater.*, 2013, **25**, 6313–6333.

47 R. Jin, C. Zeng, M. Zhou and Y. Chen, *Chem. Rev.*, 2016, **116**, 10346–10413.

48 A. Mathew and T. Pradeep, *Part. Part. Syst. Charact.*, 2014, **31**, 1017–1053.

49 A. Baksi, P. Chakraborty, S. Bhat, G. Natarajan and T. Pradeep, *Chem. Commun.*, 2016, **52**, 8397–8400.

50 Q. Yao, X. Yuan, T. Chen, D. T. Leong and J. Xie, *Adv. Mater.*, 2018, **30**, 1–23.

51 I. Chakraborty and T. Pradeep, *Chem. Rev.*, 2017, **117**,

8208–8271.
52 T. Chen, Q. Yao, R. R. Nasaruddin and J. Xie, *Angew. Chemie - Int. Ed.*, 2019, **58**, 11967–11977.
53 P. Chakraborty and T. Pradeep, *NPG Asia Mater.*, 2019, **11**, 48.
54 A. C. Templeton, W. P. Wuelfing and R. W. Murray, *Acc. Chem. Res.*, 2000, **33**, 27–36.
55 M. Zhu, C. M. Aikens, F. J. Hollander, G. C. Schatz and R. Jin, *J. Am. Chem. Soc.*, 2008, **130**, 5883–5885.
56 Z. Luo, V. Nachammai, B. Zhang, N. Yan, D. T. Leong, D. E. Jiang and J. Xie, *J. Am. Chem. Soc.*, 2014, **136**, 10577–10580.
57 J. Hassinen, P. Pulkkinen, E. Kalenius, T. Pradeep, H. Tenhu, H. Häkkinen and R. H. A. Ras, *J. Phys. Chem. Lett.*, 2014, **5**, 585–589.
58 C. M. Aikens, *J. Phys. Chem. Lett.*, 2011, **2**, 99–104.
59 A. Fernando, K. L. D. M. Weerawardene, N. V. Karimova and C. M. Aikens, *Chem. Rev.*, 2015, **115**, 6112–6216.
60 K. R. Krishnadas, A. Baksi, A. Ghosh, G. Natarajan and T. Pradeep, *Nat. Commun.*, 2016, **7**, 13447.
61 K. R. Krishnadas, A. Ghosh, A. Baksi, I. Chakraborty, G. Natarajan and T. Pradeep, *J. Am. Chem. Soc.*, 2016, **138**, 140–148.
62 A. Ghosh, D. Ghosh, E. Khatun, P. Chakraborty and T. Pradeep, *Nanoscale*, 2017, **9**, 1068–1077.
63 E. Khatun, P. Chakraborty, B. R. Jacob, G. Paramasivam, M. Bodiuzzaman, W. A. Dar and T. Pradeep, *Chem. Mater.*, 2020, **32**, 611–619.
64 S. Bhat, A. Baksi, S. K. Mudedla, G. Natarajan, V. Subramanian and T. Pradeep, *J. Phys. Chem. Lett.*, 2017, **8**, 2787–2793.
65 R. Kazan, U. Müller and T. Bürgi, *Nanoscale*, 2019, **11**, 2938–2945.
66 X. M. Lin, C. M. Sorensen and K. J. Klabunde, 2000, 157–164.
67 B. L. V. Prasad, S. I. Stoeva, C. M. Sorensen and K. J. Klabunde, *Langmuir*, 2002, **18**, 7515–7520.
68 J. R. Shimpi, D. S. Sidhaye and B. L. V. Prasad, *Langmuir*, 2017, **33**, 9491–9507.
69 D. Jose, J. E. Matthiesen, C. Parsons, C. M. Sorensen and K. J. Klabunde, *J. Phys. Chem. Lett.*, 2012, **3**, 885–890.
70 S. I. Stoeva, B. L. V. Prasad, S. Uma, P. K. Stoimenov, V. Zaikovski, C. M. Sorensen and K. J. Klabunde, *J. Phys. Chem. B*, 2003, **107**, 7441–7448.
71 P. Sahu and B. L. V. V Prasad, *Langmuir*, 2014, **30**, 10143–10150.
72 S. Stoeva, K. J. Klabunde, C. M. Sorensen and I. Dragieva, *J. Am. Chem. Soc.*, 2002, **124**, 2305–2311.
73 S. P. Bhaskar, M. Vijayan and B. R. Jagirdar, *J. Phys. Chem. C*, 2014, **118**, 18214–18225.
74 P. Sahu and B. L. V. Prasad, *Nanoscale*, 2013, **5**, 1768–1771.
75 P. Sahu and B. L. V. Prasad, *Chem. Phys. Lett.*, 2012, **525–526**, 101–104.
76 J. R. Shimpi, V. R. Chaudhari and B. L. V. Prasad, *Langmuir*, 2018, **34**, 13680–13689.
77 D. S. Sidhaye and B. L. V. Prasad, *New J. Chem.*, 2011, **35**, 755–763.
78 B. L. V. Prasad, S. I. Stoeva, C. M. Sorensen and K. J. Klabunde, *Chem. Mater.*, 2003, **15**, 935–942.
79 A. Som, I. Chakraborty, T. A. Maark, S. Bhat and T. Pradeep, *Adv. Mater.*, 2016, **28**, 2827–2833.
80 A. Chakraborty, A. C. Fernandez, A. Som, B. Mondal, G. Natarajan, G. Paramasivam, T. Lahtinen, H. Häkkinen, Nonappa and T. Pradeep, *Angew. Chemie - Int. Ed.*, 2018, **57**, 6522–6526.
81 J. Kimling, M. Maier, B. Okenve, V. Kotaidis, H. Ballot and A. Plech, *J. Phys. Chem. B*, 2006, **110**, 15700–15707.
82 A. Mari, P. Imperatori, G. Marchegiani, L. Pilloni, A. Mezzi, S. Kaciulis, C. Cannas, C. Meneghini, S. Mobilio and L. Suber, *Langmuir*, 2010, **26**, 15561–15566.
83 T. Dadosh, *Mater. Lett.*, 2009, **63**, 2236–2238.
84 Z. Wu, J. Suhan and R. Jin, *J. Mater. Chem.*, 2009, **19**, 622–626.
85 S. Bhat, R. P. Narayanan, A. Baksi, P. Chakraborty, G. Paramasivam, R. R. J. Methikkalam, A. Nag, G. Natarajan and T. Pradeep, *J. Phys. Chem. C*, 2018, **122**, 19455–19462.
86 A. Mathew, G. Natarajan, L. Lehtovaara, H. Häkkinen, R. M. Kumar, V. Subramanian, A. Jaleel and T. Pradeep, *ACS Nano*, 2014, **8**, 139–152.
87 Nonappa, T. Lahtinen, J. S. Haataja, T. R. Tero, H. Häkkinen and O. Ikkala, *Angew. Chemie - Int. Ed.*, 2016, **55**, 16035–16038.
88 E. Lee, S. S. Yi, M. S. Kim and K. Kim, *J. Mol. Struct.*, 1993, **298**, 47–54.
89 S. A. Harfenist, Z. L. Wang, M. M. Alvarez, I. Vezmar and R. L. Whetten, *J. Phys. Chem.*, 1996, **100**, 13904–13910.
90 A. Hutzler, T. Schmutzler, M. P. M. Jank, R. Branscheid, T. Unruh, E. Spiecker and L. Frey, *Nano Lett.*, 2018, **18**, 7222–7229.
91 S. Mozaffari, W. Li, M. Dixit, S. Seifert, B. Lee, L. Kovarik, G. Mpourmpakis and A. M. Karim, *Nanoscale Adv.*, 2019, **1**, 4052–4066.
92 K. Zheng, V. Fung, X. Yuan, D. E. Jiang and J. Xie, *J. Am. Chem. Soc.*, 2019, **141**, 18977–18983.
93 M. A. El-Sayed, *Acc. Chem. Res.*, 2001, **34**, 257–264.
94 W. P. Halperin, *Rev. Mod. Phys.*, 1986, **58**, 533–606.
95 C. Burda, X. Chen, R. Narayanan and M. A. El-Sayed, *Chemistry and Properties of Nanocrystals of Different Shapes*, 2005, vol. 36.
96 X. Mao, C. Liu, M. Hesari, N. Zou and P. Chen, *Nat. Chem.*, 2019, **11**, 687–694.
97 X. Zhou, W. Xu, G. Liu, D. Panda and P. Chen, *J. Am. Chem. Soc.*, 2010, **132**, 138–146.
98 P. Suchomel, L. Kvitek, R. Prucek, A. Panacek, A. Halder, S. Vajda and R. Zboril, *Sci. Rep.*, 2018, **8**, 1–11.
99 G. Kothleitner, M. J. Neish, N. R. Lugg, S. D. Findlay, W. Grogger, F. Hofer and L. J. Allen, *Phys. Rev. Lett.*, 2014, **112**, 1–5.
100 Z. Chen, M. Weyland, X. Sang, W. Xu, J. H. Dycus, J. M. LeBeau, A. J. D'Alfonso, L. J. Allen and S. D. Findlay, *Ultramicroscopy*, 2016, **168**, 7–16.
101 P. G. Kotula, D. O. Klenov and H. S. von Harrach, *Microsc. Microanal.*, 2012, **18**, 691–698.
102 S. Zhang, L. Zhang, K. Liu, M. Liu, Y. Yin and C. Gao, *Mater.*

Chem. Front., 2018, **2**, 1328–1333.
103 J. A. Manzanares, P. Peljo and H. H. Girault, *J. Phys. Chem. C*, 2017, **121**, 13405–13411.
104 L. G. AbdulHalim, M. S. Bootharaju, Q. Tang, S. Del Gobbo, R. G. AbdulHalim, M. Eddaoudi, D. E. Jiang and O. M. Bakr, *J. Am. Chem. Soc.*, 2015, **137**, 11970–11975.
105 P. Chakraborty, A. Nag, A. Chakraborty and T. Pradeep, *Acc. Chem. Res.*, 2019, **52**, 2–11.
106 K. R. Krishnadas, G. Natarajan, A. Baksi, A. Ghosh, E. Khatun and T. Pradeep, *Langmuir*, 2019, **35**, 11243–11254.
107 Q. Li, S. Wang, K. Kirschbaum, K. J. Lambright, A. Das and R. Jin, *Chem. Commun.*, 2016, **52**, 5194–5197.
108 X. Kang, S. Chen, S. Jin, Y. Song, Y. Xu, H. Yu, H. Sheng and M. Zhu, *ChemElectroChem*, 2016, **3**, 1261–1265.
109 D. K. Lee, S. Il Park, J. K. Lee and N. M. Hwang, *Acta Mater.*, 2007, **55**, 5281–5288.
110 and J. A. M. Vladimir García-Morales, Javier Cervera, ed. Klaus D. Sattler, CRC Press: Boca Raton, FL, 2011.
111 D. K. Lee and N. M. Hwang, *Scr. Mater.*, 2009, 61, 304–307.
112 A. B. Smetana, K. J. Klabunde, C. M. Sorensen, A. A. Ponce and B. Mwale, *J. Phys. Chem. B*, 2006, **110**, 2155–2158.
113 D. S. Dessau, Z. -X. Shen, B. O. Wells, W. E. Spicer, R. S. List, A. J. Arko, R. J. Bartlett, C. G. Olson, D. B. Mitzi, C. B. Eom, A. Kapitulnik and T. H. Geballe, *J. Vac. Sci. Technol. A Vacuum, Surfaces, Film.*, 1991, **9**, 383–389.
114 D. R. H. Jones, *J. Mater. Sci.*, 1974, **9**, 1–17.
115 L. Xu, W. Ma, L. Wang, C. Xu, H. Kuang and N. A. Kotov, *Chem. Soc. Rev.*, 2013, **42**, 3114–3126.
116 M. Boterashvili, T. Shirman, R. Popovitz-Biro, Q. Wen, M. Lahav and M. E. Van Der Boom, *Chem. Commun.*, 2016, **52**, 8079–8082.
117 A. Guerrero-Martínez, J. Pérez-Juste, E. Carbó-Argibay, G. Tardajos and L. M. Liz-Marzán, *Angew. Chemie - Int. Ed.*, 2009, **48**, 9484–9488.
118 K. J. Si, Y. Chen, Q. Shi and W. Cheng, *Adv. Sci.*, 2018, **5**, 1700179.
119 X. M. Lin, H. M. Jaeger, C. M. Sorensen and K. J. Klabunde, *J. Phys. Chem. B*, 2001, **105**, 3353–3357.
120 J. He, P. Kanjanaboos, N. L. Frazer, A. Weis, X. M. Lin and H. M. Jaeger, *Small*, 2010, **6**, 1449–1456.
121 J. C. Love, L. A. Estroff, J. K. Kriebel, R. G. Nuzzo and G. M. Whitesides, *Chem. Rev.*, 2005, **105**, 1103–1170.